Effect of parallel currents on drift-interchange turbulence: comparison of simulation and experiment

D. A. D'Ippolito, D. A. Russell, and J. R. Myra

Lodestar Research Corporation,
2400 Central Avenue, Boulder, Colorado 80301

S. C. Thakur, G. R. Tynan and C. Holland

Center for Momentum Transport and Flow Organization,
University of California at San Diego, San Diego, CA 92093

June, 2012

Submitted to Phys. Plasmas

DOE/ER/54392-68 LRC-12-149

Lodestar Research Corporation

2400 Central Avenue #P-5

Boulder, CO 80301

Effect of parallel currents on drift-interchange turbulence: comparison of simulation and experiment

D. A. D'Ippolito,† D. A. Russell, and J. R. Myra

Lodestar Research Corporation,
2400 Central Avenue, Boulder, Colorado 80301

S. C. Thakur, G. R. Tynan and C. Holland

Center for Momentum Transport and Flow Organization,
University of California at San Diego, San Diego, CA 92093

Abstract

Two-dimensional (2D) turbulence simulations are reported in which the balancing of the parallel and perpendicular currents is modified by changing the axial boundary condition (BC) to vary the sheath conductivity. The simulations are carried out using the 2D Scrape-Off-Layer Turbulence (SOLT) code. The results are compared with recent experiments on the Controlled Shear Decorrelation Experiment (CSDX) in which the axial BC was modified by changing the composition of the end plate. Reasonable qualitative agreement is found between the simulations and the experiment. When an insulating axial BC is used, broadband turbulence is obtained and an inverse cascade occurs down to low frequencies and long spatial scales. Robust sheared flows are obtained. By contrast, employing a conducting BC at the plate resulted in coherent (drift wave) modes rather than broadband turbulence, with weaker inverse cascade, and smaller zonal flows. The dependence of the two instability mechanisms (rotationally-driven interchange mode and drift waves) on the axial BC is also discussed.

PACS numbers: 52.35.Ra, 52.35.Kt, 52.65.Kj, 52.40.Kh

†email: **dippolito@lodestar.com**

I. Introduction

Plasma turbulence is an important area of basic physics research, and understanding edge turbulence in fusion devices is an important challenge for the future. In a toroidal device like the tokamak, turbulent transport in the edge plasma partly determines the interaction between the plasma and the first-wall and/or divertor structures. The turbulence influences the particle and heat flux to the boundary and sets the "boundary condition" (BC) for the global confinement of the core plasma. A review of edge turbulence measurements in toroidal devices is given in Ref. 1, and drift turbulence in magnetic confinement devices is reviewed in Ref 2. An important aspect of edge physics is the interaction between the turbulence and the sheared flows (see the comprehensive reviews in Refs. 3,4) The flows are driven by the turbulence through the inverse cascade process (or perhaps by nonlocal k-space interactions, loosely included in "cascades" in the following discussion), but the flows also help to saturate the turbulence and create a transport barrier, resulting in a feedback loop under some circumstances. The details of this process are being studied in tokamaks and other toroidal machines,[1-4] but can also be studied in linear machines,[5-13] which have simple geometry and good access for diagnostics. These linear experiments are also easier to simulate than fully toroidal plasmas, the difference being that turbulent structures can be independent of the coordinate along the field line and hence two-dimensional (2D) in a linear machine, but cannot be strictly so in toroidal geometry, even for an axisymmetric tokamak, because of magnetic shear.

Recently there have been a number of computer simulations of linear plasma devices,[8-13] including models with[9,10] and without[8,11-13] the sheath BC that plays an important role in the present work. These papers study basic turbulence properties, such as frequency and wavenumber spectra, direct and inverse cascades, fluctuation amplitudes, and spatial correlation lengths. Other important areas of study are the origin

of intermittency and properties of turbulent structures[8-11] and the interaction between turbulence and sheared flows.[10,12,13] In most cases, these codes do not impose a scale separation between the background plasma and the turbulence. Simulations have been compared with turbulence data from the VINETA experiment,[8-10] the Large Plasma Device (LAPD),[11] and the Controlled Shear Decorrelation Experiment (CSDX).[12] The present paper is closely related to this earlier work, and extends the modeling of CSDX to include the effect of the sheath BC on regulating the parallel currents.

Here, we discuss the effect of parallel currents on drift-interchange turbulence and flows, comparing the results of computer simulations with data from recent experiments on CSDX. To motivate this work, we note that the vorticity equation enforces current conservation and thus controls the flow of perpendicular and parallel currents. In linear plasma devices, where the field lines terminate on material boundaries, the magnitude of the parallel current $J_{||}$ (and the ratio $J_{\perp}/J_{||}$) is controlled by the axial BC. For example, when the end plates are conducting, a sheath allows, but also limits, the parallel current to the end plates and influences the linear stability and related turbulence.[14-18] Recently, this issue was studied on CSDX[19] by changing the composition of the end plates in order to modify the axial BC. The characteristics of the plasma turbulence were measured for both an insulating boundary condition (IBC) and a conducting boundary condition (CBC),[19] and were found to be quite different in the two cases. These experiments motivated simulations using the two-dimensional (2D) Scrape-Off-Layer Turbulence (SOLT) code,[20-23] which can treat both insulating ($\alpha_{sh} = 0$) and conducting ($\alpha_{sh} \neq 0$) cases by varying the strength of a sheath conductivity parameter α_{sh} defined in Sec. II. The two dimensions modeled dynamically in SOLT are the coordinates perpendicular to the magnetic field. The present paper describes these simulations and compares the simulation and experimental results.

Not only the magnitude, but also the nature of the turbulence, should depend on the axial BC. In nonlinear edge and scrape-off-layer (SOL) turbulence, the perpendicular

current includes the ion polarization drift term responsible for the inverse energy cascade, so it is reasonable to expect that the nature of the turbulence will depend on how this term balances the parallel current flow. A similar situation arises in the study of blobs, where the competition between the polarization drift and parallel current terms influences parallel disconnection and the blob velocity.[18,24,25] While a full study of the inverse cascade is beyond the scope of this paper, we will discuss the qualitative differences between the turbulence in the IBC and CBC cases.

We will show that there are several points of qualitative agreement between our simulations (see Sec. IV) and the experiment (see Sec. V and Ref. 19), including the following:

1. The insulating (IBC) case is characterized by broadband turbulence and inverse cascade down to zero frequency ($\omega = 0$) and to long spatial scales (low k_y), thereby driving sheared flows;
2. The conducting (CBC) case is dominated by coherent modes; there is reduced broadband turbulence, a weaker inverse cascade to low ω and k_y, and weaker low-frequency zonal flows;
3. The Reynold's stress profiles are different for the IBC and CBC cases;
4. The azimuthal velocity resulting from turbulent Reynold's stress interactions is larger in the IBC case than in the CBC case.

The CSDX experiments are also useful for testing basic simulation issues, such as the type of sources and sinks and the boundary conditions, and validating the code for 2D geometry. The 2D SOLT code has been used with some success to model edge turbulence in tokamaks.[22,23,26] This turbulence is inherently three-dimensional (3D) due to magnetic shear (e.g. X-points) which can force the turbulence to vary along the field lines. This is treated only approximately in a 2D model by various closure relations. So, it is interesting and useful to test the computational model in a context where true 2D turbulence is a more realistic ansatz. However, the SOLT code uses slab geometry,

whereas the CSDX experiment is a cylindrical device. Near the axis of the cylinder (r = 0) the slab description will not be very accurate. For purposes of studying gradient-driven turbulence (which peaks near the plasma edge), we expect that the slab model will be adequate, but the difference in geometry means that we can only expect qualitative, not quantitative, agreement between theory and experiment.

The plan of this paper is as follows. In Sec. II we discuss the relevant time scales for physical processes that control the flow of charge. This allows us to understand analytically the two regimes corresponding to the insulating and conducting BCs, and it introduces the dimensionless parameters of the SOLT code. In Sec. III the computational model is briefly described. Simulation results are given in Sec. IV and are compared with experimental data in Sec. V. Finally, Sec. VI gives a summary and discussion of these results.

II. Physical regimes

As noted in the previous section, the physics of edge turbulence can be understood by the balancing of terms in the vorticity equation, which is equivalent to the current conservation constraint that $\nabla \cdot \mathbf{J} = 0$. There are four relevant time scales. The first is the time scale for $\mathbf{E} \times \mathbf{B}$ advection of charge by the ion polarization drift ($\sim \mathbf{v} \cdot \nabla \nabla^2 \Phi$), which is given by

$$\tau_{adv}^{-1} \sim \mathbf{v} \cdot \nabla \sim \frac{c}{B} \frac{\Phi}{L_\perp^2} \sim \varpi \tag{1}$$

where $\varpi = \nabla \times \mathbf{v}$ is the vorticity and also gives the rate of advection, and $L_\perp$ is the perpendicular scale length of the turbulence. Here **v** is the E×B velocity, c is the speed of light and **B** is the magnetic field. The second time scale is that of charge separation by an external force $\mathbf{F} = n m_i \mathbf{g}$ (e.g. curvature or centrifugal forces which can be modeled as an "effective gravity" **g**), where n is the plasma density and m_i the ion mass. This time

scale can be estimated from the ideal interchange growth rate $\gamma \sim (g/L_n)^{1/2}$ using $L_n \sim L_\perp$ to obtain

$$\tau_g^{-1} \sim \left(\frac{g}{L_\perp}\right)^{1/2} \sim \varpi \tag{2}$$

where $g \sim v_\theta^2 / r$ for the centrifugal force, which is the dominant force in CSDX.

There are also time scales related to charge loss by parallel currents. We can estimate the parallel loss time τ_ρ for charge density $\rho = n\,e$ from $\partial\rho/\partial t \sim \nabla_\parallel J_\parallel$, viz. $\tau_\rho^{-1} \sim J_\parallel / \rho L_\parallel$. On open field lines where sheath effects are important, the time scale for charge loss by parallel currents to sheaths ($\tau_\rho \to \tau_{sh}$) can be estimated using the sheath relation $J_\parallel = nec_s(e\Phi/T) = \omega_{pi}^2\Phi/(4\pi c_s)$ with $4\pi\rho = \varepsilon_\perp \nabla_\perp^2 \Phi$ and $\varepsilon_\perp = \omega_{pi}^2/\Omega_i^2$ (the polarization screening, where c_s is the sound speed, T the electron temperature, ω_{pi} the ion plasma frequency and Ω_i the ion cyclotron frequency) to obtain

$$\tau_{sh}^{-1} \sim \frac{J_\parallel}{\rho L_\parallel} \sim \frac{L_\perp^2}{\tau_\parallel \rho_s^2}\ , \tag{3}$$

where $\tau_\parallel = L_\parallel / c_s$, $\rho_s = c_s/\Omega_i$. This effect enters the vorticity equation in the SOLT code via a sheath boundary condition at the axial points $z = \pm L_\parallel$ where the field lines hit the metal boundaries, and this BC depends on the parallel connection length $L_\parallel$ to the sheaths. The sheath BC enters the 2D SOLT model when the vorticity equation is averaged along the magnetic field in the SOL to obtain a 2D model.

The SOLT code also contains a model for the parallel current in the closed field line (edge) region, viz. a Hasegawa-Wakatani type model for incorporating collisional drift wave effects.[27] When drift wave effects are important, the modes have parallel variation along the field lines ($k_\parallel \neq 0$), and the parallel current due to the drift wave perturbation is estimated as $\nabla_\parallel J_\parallel \sim \alpha_{dw}(nec_s/\rho_s)(e\Phi/T)$, where

$$\alpha_{dw} \equiv \frac{2k_{\|}^2 \rho_s c_s m_i}{\nu_{ei} m_e} \rightarrow \frac{2\rho_s c_s m_i}{L_{\|}^2 \nu_{ei} m_e} = \frac{2\rho_s}{L_{\|}\Lambda} \quad , \tag{4}$$

$$\Lambda = \frac{\nu_{ei} L_{\|}}{\Omega_e \rho_s} \quad . \tag{5}$$

Here, in the second form of Eq. (4) we make the approximate identification $k_{\|} \rightarrow 1/L_{\|}$, and in the third form we introduce $\Lambda = (m_e/m_i)^{1/2} \nu_{*e} \equiv (m_e/m_i)^{1/2} (L_{\|}/\lambda_{ei})$, a collisionality parameter used in recent blob modeling.[25] Using the drift wave parallel current, we can estimate the parallel loss time due to drift wave turbulence ($\tau_{\rho} \rightarrow \tau_{dw}$),

$$\tau_{dw}^{-1} \sim \frac{J_{\|}}{\rho L_{\|}} \sim \frac{1}{\tau_{\|}\Lambda} \frac{2L_{\perp}^2}{\rho_s^2} \quad . \tag{6}$$

Comparing Eqs. (3) and (6), we find that drift wave effects compete with sheath effects when $\Lambda \sim 1$, which is typical of CSDX parameters in the conducting regime.

The main point of the experiments modeled here is to explore the effect of changing the characteristics of the end plates from the insulating (IBC) to conducting (CBC) regime. To quantify this transition analytically, we compare three time scales. The inertial, interchange, and sheath (~ drift-wave) inverse time scales stand in the ratio

$$\varpi \; : \; \frac{g}{\varpi L_{\perp}} \; : \; \frac{L_{\perp}^2}{\tau_{\|} \rho_s^2} \; . \tag{7}$$

Here, the notation A : B : C means that A, B and C are typical terms that compete in the equation, and a maximal ordering will have A ~ B ~ C. Equating the first two time scales results in the characteristic (time, vorticity and/or potential) scale $\varpi \sim (g/L_{\perp})^{1/2}$, which is just the second relation in Eq. (2). Equating all three terms gives the following critical connection length

$$L_{\|c} = \left(\frac{L_{\perp}^5 c_s^2}{g \, \rho_s^4} \right)^{1/2} \quad , \tag{8}$$

which demarcates the transition from insulating ($L_{\|} >> L_{\|c}$) to conducting ($L_{\|} \le L_{\|c}$) boundary conditions when the boundary plate itself is not explicitly an insulator. Here, the insulating (conducting) regime is characterized analytically as having a small (large) sheath term. Also recall that the drift wave and sheath time scales scale similarly, so that the limiting cases in the insulating (conducting) regimes correspond to having interchange (drift wave) drive as the dominant effect.

In dimensionless Bohm units (with all lengths normalized to ρ_s and velocities normalized to c_s) and with $g \sim v_\theta^2 / r$, Eq. (8) becomes $L_{\|c} = \left(r L_\perp^5 / v_\theta^2 \right)^{1/2}$. Thus, for a fixed $L_{\|}$, this scaling argument predicts that large (small) azimuthal velocities correspond to perturbations which are disconnected (connected) electrically to the end plates and thus to the IBC (CBC) regimes. This result agrees qualitatively with both the simulations and the experimental data (as discussed further in Sec. V).

The overall point of this discussion is the following. When conducting end-plates are employed, so as not to forbid parallel currents outright, the sheath itself can either act as an insulating or conducting end-wall boundary condition, according to Eq. (8). When insulating end-plates are employed, the electrical characteristics of the sheath are not relevant. In the SOLT simulations which follow, we legislate the sheath to be insulating for the IBC simulations, but allow the sheath conductivity to take its natural value for CSDX parameters in the CBC case. This value turns out to permit substantial parallel currents, i.e. $L_{\|} \le L_{\|c}$.

As an aside, we note that in the toroidal-curvature-driven (e.g. tokamak) case (with $g \sim c_s^2 / R$), solving Eq. (8) for $L_\perp$ gives the usual characteristic blob scale length $L_\perp = \delta_*$ that separates the inertial ($\delta << \delta_*$) from the sheath-connected ($\delta >> \delta_*$) regimes.[24,25] However, when the turbulence is rotationally-driven ($g \sim v_\theta^2 / r$) and the radial scale $L_\perp$ of the turbulence is insensitive to the axial BC, Eq. (8) becomes a condition on the parallel scale length.

III. SOLT model

The 2D SOLT code[20-23] simulates electrostatic fluid turbulence driven by external forces (e.g. magnetic curvature or centrifugal force), velocity shear and drift waves in a plane perpendicular to the magnetic field **B**. The physics model includes turbulent radial transport (turbulent Reynolds stress and blobs), sheared flow effects (KH instability and velocity-shear stabilization), and sheath dissipation of particles, energy and momentum. The simulation domain is the radial-azimuthal plane of the cylindrical CSDX plasma, averaged along field lines. Thus, the code is "global" (not a flux-tube model) and allows flexibility in setting up the transition from the core to the wall using reference profiles described below. The simulation plane is denoted as the (x, y) plane, where x is the radial distance from the center of the plasma (r = 0), and y is the binormal (approximately azimuthal) coordinate. The B field is in the z direction. We note that the density profile in the simulation is specified all the way to x = 0, but it is a slab model without cylindrical coordinate Jacobian factors, so one cannot take the inner part (near the origin) very seriously. We will discuss this point further.

The physics of the model is described in an earlier paper,[21] and a derivation of the equations is given in the Appendix of that paper. Here, we give only a brief summary of the model. The fundamental equations in the SOLT model are the vorticity, continuity and energy conservation (temperature) equations. In the present study, we simplify the model by assuming a constant temperature profile. Thus, the model reduces to the following equations:

$$\frac{d}{dt}\nabla\cdot n\nabla\Phi = A_{dw}(\Phi,n) + \alpha_{sh}J_{||} - \frac{\beta}{n}\frac{\partial(nT)}{\partial y} \tag{9}$$

$$\frac{dn}{dt} = A_{dw}(\Phi,n) - \alpha_{sh}\left(nT^{1/2} - J_{||}\right) \tag{10}$$

The convective derivative is written as $d/dt = \partial/\partial t + \mathbf{v}\cdot\nabla$ where $\mathbf{v} = \mathbf{e}_z \times \nabla\Phi$. Here, all quantities are made dimensionless using Bohm units, viz. inverse time-scales are normalized to $\Omega_{ci} = ZeB/m_i c$ and space scales to $\rho_{sr} = c_{sr}/\Omega_{ci}$, where $c_{sr}^2 = T_{er}/m_i$ and T_{er} is a reference temperature. The electron density $(n \to n/n_{er})$ and parallel current $(J_{||} \to J_{||}/n_{er}\, e\, c_{sr})$ are normalized using a reference density n_{er}. In the present work, the temperature is taken to be a constant, so that $T \equiv T_e/T_{er} \to 1$ in these equations.. The dimensionless force parameter β is defined as $\beta = (v_\theta^2/c_s^2)(\rho_s/r)$ and thus the last term on the right hand side (RHS) of Eq. (9) provides the interchange drive for the turbulence.

Analytical closure relations are employed to describe the parallel dynamics in these equations. A number of closures have been used in previous work. Here, when $\alpha_{sh} \equiv (2\rho_s/L_{||})$ is large the relationship of parallel current $J_{||}$ to Φ is prescribed by a sheath closure, $J_{||} = nT^{1/2}(1 - e^{(\Phi_B - \Phi)/T})$, where $\Phi_B \sim 3$ T is the Bohm sheath potential. The parameter α_{sh} is called the sheath conductivity. Additionally, an adiabaticity model for $J_{||}$ is employed to capture basic drift-wave physics from the parallel electron dynamics, which dominates when $k_{||}$ is large or ν_{ei} is small. This results in the terms with the drift wave operator A_{dw}, defined by

$$A_{dw}(\Phi, n) = \alpha_{dw}\overline{T}^{3/2}\{\Phi - T\ln n\}, \tag{11}$$

where $\overline{Q} \equiv < Q >$ is the zonal or y-averaged part, and $\widetilde{Q} \equiv \{Q\} = Q - \overline{Q}$ is the fluctuating part, of any quantity Q. The parameter α_{dw} is defined in Eq. (4). The operator A_{dw} enforces a Boltzmann response on fluctuations when the coefficient α_{dw} is large, in the spirit of the Wakatani-Hasegawa adiabaticity parameter.[27] The term on the left hand side of Eq. (9) comes from the ion polarization drift.

To summarize, the important physics parameters in the SOLT model are

$$\beta = \frac{v_\theta^2}{c_s^2}\frac{\rho_s}{r} \quad , \quad \alpha_{dw} = \frac{2\rho_s}{L_{||}\Lambda} \quad , \quad \alpha_{sh} = \frac{2\rho_{sr}}{L_{||}} \quad , \tag{12}$$

where $\Lambda = (m_e / m_i)^{1/2}(L_{\|} / \lambda_{ei})$ is a collisionality parameter. Here β is the centrifugal-force parameter, α_{dw} is the electron adiabaticity (drift wave) parameter, and α_{sh} is the sheath conductivity parameter, where $L_{\|}$ is the midplane-to-divertor-plate connection length in the SOL. If we tried to match the experimental profiles, then β, α_{dw}, and α_{sh} would be functions of x. Here, for simplicity, we take each of these profiles to be constant in radius and use a typical value.

The SOLT code solves the vorticity equation, by splitting Eq. (9) into zonally-averaged and fluctuating parts. The zonally-averaged part is manipulated into a conservative form for zonal (i.e. y) momentum conservation. The Boussinesq approximation is employed on the fluctuating part. Small diffusive terms are usually added to Eqs. (9) – (10) to absorb high-wavenumber fluctuations before they cascade to the scale of the numerical grid.

The model equations are solved subject to the following set of boundary conditions: (1) azimuthal (y) periodicity is assumed; (2) fluctuations are forced to vanish ($\tilde{n} = \tilde{\Phi} = 0$) on the left and right boundaries in x; (3) $\overline{v}_y \equiv \partial_x \overline{\varphi} = 0$ on the core side (left) boundary; and (4) $\overline{\varphi} = 3\overline{T}$ is imposed at the radial wall (right hand boundary in x).

Finally, it is important to discuss the sources and sinks in the CSDX simulations. To obtain an effective particle source and sink, we force the density profile to relax to a reference density profile $n_0(x)$, where the latter is based on experimental data. This requires an extra term in the continuity equation of the form $\nu_n(n - n_0)$. The temperature is specified to be constant in x and t at the experimentally measured value (T_e = 3 eV). Note that the velocity profile $v_y(x) = \partial_x \Phi$ is free to evolve in this simulation (except at the left boundary) and gives another point of comparison with the experiment.

IV. Simulation Results

In this section, we compare SOLT simulation results for the insulating (IBC) and conducting (CBC) cases. For the IBC case, the experiment[19] shows strong turbulence

and associated flows, and there is some evidence for drift wave effects. There are no sheaths in the insulating limit. The IBC case is modeled by the following choice of dimensionless physics parameters: $\beta = 0.01$, $\alpha_{dw} = 0.01$ and $\alpha_{sh} \equiv 0$. For the conducting boundary experiments, the flows are much weaker, drift wave effects are important, and sheath formation is expected. Thus, the CBC case is modeled by $\beta = 0.0025$, $\alpha_{dw} = 0.01$ and $\alpha_{sh} = 0.01$. Note that the centrifugal force parameter was reduced by a factor of 4 in the CBC case to model the reduced flows. In both cases, the density relaxation parameter is $\nu_n = 0.05$.

A. Basic properties

A representative selection of results from the IBC simulation is shown in Fig. 1 and results from the CBC simulation are shown in Fig. 2. Here, the notation $< \overline{Q} >_t \equiv < Q >_{y,t}$ denotes the y- and t-averaged quantity, where y is the zonal average. In part (a), the average density profile is shown, and the vertical lines (which appear as dots) denote the standard deviation of the fluctuations about the mean. The fluctuations are small partly because the density relaxation rate ν_n is large ($\nu_n / \alpha_{dw} \sim 5$). In both cases the density profile relaxes to the reference profile $n_0(x)$, which is a tanh fit to the experimental density profile. Note that the scales of the two plots are different; the density is smaller in the CBC case because of particle losses to the sheath (particle loss rate $= 1/\tau_{sh} \propto \alpha_{sh}$).

In part (b) the radial dependence of the average velocity profile is shown. The sheared velocity profile is the result of the self-consistent evolution of the turbulent fluctuations. Note that the $< \overline{v}_y(x) >_t$ profile has two lobes and the fluctuations (indicated by vertical lines) are large. The positive velocity lobe agrees with the flow direction observed in the experiment. The existence of two lobes in the simulation is due to azimuthal momentum conservation and the chosen initial condition for the azimuthal velocity. The simulations are initialized with $\overline{v}_y(t = 0) = 0$ at all x, so by momentum

conservation the radially-integrated density-weighted velocity must vanish. This requires the dipole structure of $< \bar{v}_y(x) >_t$ observed in part (b) of Figs. 1 and 2. The experiment may not conserve azimuthal momentum to the same degree as the simulations due to dissipation, e.g. from ion-neutral drag effects,[28] and thus have only the positive velocity lobe. Also, cylindrical geometry (not modeled here) will affect the weighting of the azimuthal momentum, to the extent it is conserved.

The maximum azimuthal velocity in the simulation is about 400 m/s for the IBC simulation, compared with 950 m/s in the IBC experiment. In the simulations, the maximum $< \bar{v}_y >_t$ is much larger for the insulating case than for the conducting case, in qualitative agreement with the experiment. (This also justifies after the fact the choice of a reduced value of $\beta \propto v_\theta^2$ in the CBC simulation.) We also plot the radial profile of the zonally-averaged Reynold's Stress (RS), $< v_x v_y >_{y,t}$, for the two cases in part (c) of Figs. 1 and 2. As in the experiment, the simulations of the two cases show that the radial profiles of the RS have different shapes; the magnitude is similar but the signs are different for the IBC and CBC cases. Thus, the axial BC strongly influences the azimuthal flows.

In part (d) we plot the frequency spectrum of the potential fluctuations $<|\phi(\omega)|^2>_y$ at a fixed radial point (x = 3.8 cm). Note the logarithmic scale of the fluctuations. Here, the underlying physics becomes more visible. The IBC case is characterized by broadband turbulence with an inverse cascade, leading to sheared flows at $\omega = 0$. In contrast, the CBC case has discrete modes and much less activity near $\omega = 0$. Note that this behavior persists over five orders of magnitude. The presence or absence of the inverse cascade in the two cases may partly explain why the flows are so much larger in the insulating case. The time dependence of the RS is shown as an inset to the frequency spectra. This shows the same features (broadband turbulence in Fig. 1 vs. discrete, quasi-periodic modes in Fig. 2). These results are qualitatively consistent with the results obtained in the CSDX experiment.[19]

In part (e) of these figures, we show the wavenumber spectrum of the potential fluctuations $<|\phi(k_y)|^2>_t$ at a fixed radial location, x = 3.8 cm. In the IBC case, the mode driving the turbulence occurs at $k_y = 0.6\ \text{cm}^{-1}$; the inverse cascade then enhances the mode at $k_y = 0.3\ \text{cm}^{-1}$, but this does not occur in the CBC case. Thus, both the frequency and wavenumber spectra show the characteristics of the nonlinear cascade in the IBC case. The peak value of k_y can be compared in the simulation and the experiment. In the latter, the dominant mode is m = 3, the plasma radius is *a* = 6 cm and the associated wavenumber is $k_\theta = m/a = 0.5\ \text{cm}^{-1}$, which is close to the value $k_y = 0.6\ \text{cm}^{-1}$ in the simulation.

In part (f), we show an (x,y) contour plot of the potential fluctuations near the end of the simulation, in the saturated turbulent state. The contour plot shows the spatial patterns reflecting the different dominant modes in the two cases.

B. Dominant physics

A term-by-term analysis of the energy budget, derived from the vorticity equation, in the simulation allows us to understand the dominant physical processes in both cases discussed in the previous section. In Fig. 3, the following quantities are plotted for both the IBC (solid line) and CBC (dashed line) cases: (a) the wavenumber spectrum of the total kinetic energy, $<|\mathbf{v}_k|^2>_{x,t}$, where k = k_y; (b) the centrifugal forcing term in the vorticity equation, proportional to β; (c) the sheath term, proportional to α_{sh}; (d) the nonlinear (NL) term $<\mathbf{v}\cdot\nabla(\nabla^2\Phi)>_{x,t}$, which is responsible for the mode coupling and inverse cascade of the energy; (e) the drift wave term, proportional to α_{dw}; and finally (f) a dissipation (viscosity) term, $\mu\nabla^4\Phi = \mu\nabla^2\varpi$, which was used in these simulations. All terms in Fig. 3 are averaged over x and t. The x average is justified because the dominant modes fill the computational domain, and the time average is taken over the last half of the simulation run in order to exclude initial transient effects.

In part (a) note that the k_y spectrum of $<|\mathbf{v}_k|^2>_{x,t}$ peaks at the second wavenumber for both IBC and CBC cases, but the behavior as $k_y \to 0$ is quite different for the two boundary conditions. Only the insulating case shows evidence of sheared zonal flows due to inverse cascade from higher k.

An analysis of parts (b) to (f) of Fig. 3 leads to the following physical picture. In the insulating case, the instability is driven by both the rotational ($\propto \beta$) and the drift wave ($\propto \alpha_{dw}$) drives. These are balanced by damping from the nonlinear term and from the dissipation term ($\propto \mu$). The nonlinear term takes energy away from the dominant mode and transfers it to the sheared flows by inverse cascade. The viscosity term dissipates high-k modes produced by the forward cascade of vorticity. It should be noted that the drift wave drive (with linear growth rate $\gamma \propto L_n^{-1}$) is stronger than the rotational drive ($\gamma \propto L_n^{-1/2}$) for these parameters. This typically occurs when the density gradient is steep, as in the present simulations.

Turning to the conducting case in Fig. 3, we see that the drift wave provides the dominant instability drive and the energy sinks are provided by the sheath and viscosity terms. The power budget analysis shows that the sheath term is very important in the CBC case, whereas it plays no role ($\alpha_{sh} = 0$) in the IBC case. The presence of sheath dissipation diminishes the inverse cascade and the development of sheared azimuthal flows in the simulation. In both the insulating and conducting cases, the drift wave instability drive is important in the simulations, as it is in the CSDX experiment.

V. Experimental results

In this section, we will illustrate some of the main points of comparison between the theory (Sec. II), the simulations (Sec. IV) and the CSDX experimental data (Ref. 19). Some pertinent figures from Ref. 19 are reproduced here for the reader's convenience.

A dimensional analysis in Sec. II gave conditions for the sheath term to be in the insulating and conducting limits. The insulating BC is appropriate when the end plate is

covered with an insulating material or when $L_{||} >> L_{||c}$ (for the case where the conducting end plate is covered by a plasma sheath). In the latter case, the sheath imposes a conducting BC when $L_{||} \le L_{||c}$, where $L_{||}$ and $L_{||c} = \left(rL_{\perp}^{5} / v_{\theta}^{2}\right)^{1/2}$ are given in Bohm units. We have estimated the ratio $L_{||} / L_{||c}$ for the CBC cases using the experimental parameters to show that in fact it should behave in the conducting limit. In Fig. 4, the experimental data for the measured azimuthal velocity profile, $v_{\theta}(r)$, is shown for both cases, and allows us to estimate the radius r (taken to be the point where v_{θ} peaks) and the perpendicular scale length $L_{\perp}$. For the CBC case, the parameters are r = 3 cm, $L_{\perp} = 2$ cm, and $v_{\theta} = 5 \times 10^{4}$ cm/s. The parameters which were held fixed for both cases are $L_{||} = 280$ cm, B = 1 kG, T_e = 3 eV, Z = 1 and $\mu = 18$ (Argon gas), where Z is the charge state and $\mu \equiv m_i / m_p$ is the ion / proton mass ratio. The result of this analysis is that $L_{||} / L_{||c} \approx 2$ for the conducting case. Thus, to within a factor of 2, the experimental data confirms at the heuristic level of the theoretical estimates in Sec. II that the CBC case is indeed in the conducting limit and therefore significant differences in behavior should be expected in the CBC and IBC cases.

We now turn to a comparison of the experimental and simulation profiles. In Fig. 4, the radial profile of v_{θ} is computed using Time Delay Estimation (TDE) methods. Azimuthal **E**×**B** velocities calculated from swept Langmuir probe measurements of the plasma potential (not shown here) give results quite close to the TDE results. In the simulations, v_{θ} is obtained directly by taking both time- and azimuthal-averages over the turbulence of the azimuthal component of cE_x / B. In Fig. 4 the main feature of interest here is that the peak v_{θ} is significantly larger for the IBC case than for the CBC case. These profiles are to be compared with the simulation results shown in part (a) of Figs. 1 and 2. Specifically, we compare the positive velocity lobe in the simulation with the positive lobe in the experimental data, looking for qualitative trends. In both experiment and simulation, the azimuthal velocity is stronger in the IBC case.

The ratio of the peak velocities for the IBC / CBC cases is about two in the experiment and four in the simulation. Better agreement for this ratio could have been obtained by optimizing the values of the parameters in the simulation, but this was not intended to be a quantitative study. For a qualitative study, this factor of 2 agreement is reasonable. The physical reasons for the difference between the IBC and CBC cases were discussed in Sec. IV.B, based on an analysis of the various physical terms in the turbulence simulation.

Finally, we note again that the radial location of the peak velocity differs between the simulation and the experiment. Possible reasons for this difference were discussed in Sec. IV.A in connection with Fig. 1(a).

The experimental Reynold's stress (RS) radial profiles, $< v_r v_\theta >$, are shown in Fig. 5, which is to be compared with the profile of $< v_x v_y >$ in part (c) of Figs. 1 and 2. Both the experiments and simulations have a larger RS in the insulating BC case than in the conducting BC case. Another point of agreement is that the peak RS in the IBC case is about 10^9 $cm^2\, s^{-1}$ for both simulation and experiment.

One difference between the simulation and experimental results is that the RS data in the simulation [Fig. 1(c) and 2(c)] is not filtered, whereas the experimental data (Fig. 5) uses a pass-band filter that removes the low frequency (< 5 kHz) fluctuations associated with the sheared flow and retains the frequency range (5 kHz < f < 30 kHz) associated with the drift waves[29-31] Applying a similar pass-band filter to the simulation data shows that the mean value of the RS is not affected very much by the filtering, but the standard deviation is reduced as the allowed frequency range is reduced. Comparing cases with similar filtering, we note that the standard deviation of the RS fluctuations is larger in the simulation than in the experiment, indicating that in some sense the simulation is more robustly turbulent. We did not show the filtered results for the simulation because they are basically similar to the unfiltered results.

Finally, in Fig. 6 we show the experimentally-obtained frequency spectra for the plasma floating potential fluctuations in the IBC and CBC cases. These figures are to be compared with part (d) of Figs. 1 and 2. The same qualitative character is evident in both experiment and simulation. In the case of the insulating boundary, there is strong broadband turbulence and an inverse cascade to low frequency (and long scale lengths, coupling to the sheared flows). With a conducting boundary, the turbulence is replaced by discrete modes which have a drift wave character, and there is no cascade to low frequencies. In both the simulation and the experiment, the peak fluctuations occur in the frequency range 5 – 10 kHz. The radial dependence of these frequency spectra are shown in Fig. 7 of Ref. 19, confirming that the behavior described here is global in nature.

VI. Summary and Discussion

In this paper, we have studied the influence of the axial boundary condition (and hence parallel currents) on drift-interchange turbulence in CSDX, a linear plasma device with turbulence that is quasi-two-dimensional. This study compared the results of analytic work (Sec. II) and numerical simulations (Sec. IV) with experimental data[19] (Sec. V). The simulations used the SOLT code,[20-23] which is well-suited to studying the effect of parallel BCs on turbulence (Sec. III).

The analytic estimates yielded a condition [see Eq. (8)] for a critical parallel connection length $L_{\|c} = \left(rL_{\perp}^{5} / v_{\theta}^{2}\right)^{1/2}$, where all lengths are normalized to ρ_s and velocities normalized to c_s. For $L_{\|} >> L_{\|c}$, or when endplates are explicitly insulating, the theory predicts a regime in which the sheath and drift wave physics is weak and the azimuthal flow velocity is strong. For $L_{\|} \le L_{\|c}$, the theory predicts that the sheath and drift wave terms are dominant and the azimuthal flow velocity is weak. This analytic result was found to hold qualitatively in both the SOLT simulations and the CSDX experimental results. For the present experiment, we estimate $L_{\|} / L_{\|c} \approx 2$ for the

conducting case, so that the use of a conducting endplate should significantly alter the dynamics, as observed in both simulation and experiment.

Regarding the simulation, the strongest point of agreement was the effect of the axial BC, as just described. The weakest aspect was the computed behavior at x = 0, which corresponds to the origin (r = 0) in the cylindrical experiment. The velocity v_y has a negative lobe at small x in both Figs. 1(b) and 2(b) which is not present in the experimental data. The dipole structure of v_y (in x) was attributed to momentum conservation, although the different behavior of slab and cylindrical coordinates near the origin may also play a role. It is possible that implementing cylindrical geometry in the SOLT code would have eliminated this discrepancy, but this lies outside the scope of this paper. Published analysis of these experments[28] has also shown that ion-neutral drag can be important, particularly in the boundary region, and allows the plasma to exchange momentum with the laboratory. These effects also lie outside the scope of this comparison and are not included in the modeling presented here.

Despite the difference in geometry, there is qualitative agreement between experiment and simulations concerning the role of the axial BC. In the simulations, the plasma with an *insulating* axial boundary showed a greater fluctuation level, broadband turbulence, and inverse energy cascade with development of sheared azimuthal flows. The plasma with a *conducting* axial boundary had a lower fluctuation level, quasi-periodic (coherent) mode activity, weak inverse cascade and weak flows. All of these features agree with the experimental observations described in Ref. 19. We note in passing that these results suggest that linear experiments with an insulating axial boundary are better suited to studies of turbulent cascades and sheared flow generation than those with conducting boundaries.

In both the insulating and conducting cases, the simulations showed that the main driver for the turbulence was the drift wave physics, although rotational (centrifugal) drive also played a role. The main difference between the IBC case and the CBC case

with $L_{||} \le L_{||c}$ was the effect of the sheath in the latter case, viz. shorting out the DC and turbulent electric fields in the plasma by allowing current flow to the plate. The simulations confirm that the sheath dissipation plays an important role by stabilizing the broadband turbulence and thus diminishing the inverse cascade and formation of sheared flows.

The difference between the insulating and conducting cases can also be understood in terms of current conservation. The integrated sheath term in the vorticity equation [Eq. (9)] describes the $\mathbf{J} \times \mathbf{B}$ force from the radial current in the current loop implied by $\nabla \cdot \mathbf{J} = 0$. Thus, the parallel current flow into the sheaths must balance this radial current, $\langle J_x \rangle = \int_x^{L_x} dx' \langle \nabla_{||} J_{||} \rangle$, where $J_{||} \propto \alpha_{sh} \Phi$ and the brackets indicate a field line average. This sheath-generated radial current opposes the polarization drift current driven by the Reynolds stress. Thus, polarization drift effects, such as the development of broadband turbulence and inverse energy cascade to produce sheared azimuthal flows, are weaker when sheath currents are present.

The comparison of simulation and experiment in this paper is interesting from several points of view. First, it represents an initial attempt at SOLT code validation against a plasma device with quasi-2D turbulence. With the density profile forced to relax to near its experimental value, the azimuthal velocity profile evolved self-consistently in the simulation (driven by the Reynolds' stress) to achieve a maximum flow velocity similar to that in the experiment. The density profile relaxation (equivalent to specifying the particle sources and sinks) was essential to obtaining the correct evolution of the velocity. This is an example of a general property of turbulence simulations: it is crucial in modeling experiments to use the correct sources and sinks and to avoid arbitrarily defining an equilibrium and then computing fluctuations about that fixed equilibrium. Second, this work demonstrates that the nature of the turbulence (e.g. strength of the inverse cascade) is sensitive to the detailed balancing of the parallel and perpendicular

currents, and thus to the axial boundary condition seen by the turbulence. This result has also been seen in studies of blob propagation.[24,25]

Acknowledgements

We would like to thank Min Xu, Peter Manz, and Nicolas Fedorczak for useful discussions. This work was supported by the U.S. Department of Energy (DOE) under DOE Grants No. DE-FG02-97ER54392 and DE-FG02-06ER54871; however, this support does not constitute an endorsement by the DOE of the views expressed herein.

Figure Captions

Fig. 1 (Color online) Numerical results from a SOLT simulation of CSDX with the *insulating* axial boundary condition: (a) radial profile of the average density, $<\bar{n}>_t$; (b) radial profile of the average azimuthal velocity, $<\bar{v}_y>_t$; (c) radial profile of the average Reynold's stress, $<v_x v_y>_{y,t}$; (d) frequency spectrum of potential fluctuations $<|\phi(\omega)|^2>_y$ at a fixed radial point (x = 3.8 cm); wavenumber spectrum of potential fluctuations $<|\phi(k_y)|^2>_t$ at x = 3.8 cm; and (f) contour plot in (x,y) plane of the potential fluctuations near the end of the simulation run (t = 56 ms). Here, $<\overline{Q}>_t \equiv <Q>_{y,t}$ denotes the zonally- and time-averaged value of any quantity Q.

Fig. 2 (Color online) Numerical results from a SOLT simulation of CSDX with the *conducting* axial boundary condition: (a) radial profile of the average density, $<\bar{n}>_t$; (b) radial profile of the average azimuthal velocity, $<\bar{v}_y>_t$; (c) radial profile of the average Reynold's stress, $<v_x v_y>_{y,t}$; (d) frequency spectrum of potential fluctuations $<|\phi(\omega)|^2>_y$ at x = 3.8 cm; (e) wavenumber spectrum of potential fluctuations $<|\phi(k_y)|^2>_t$ at x = 3.8 cm; and (f) contour plot in (x,y) plane of the potential fluctuations near the end of the simulation run (t = 80 ms).

Fig. 3 Wavenumber spectrum of the terms in the vorticity equation for simulations with the insulating axial BC (solid line) and the conducting axial BC (dashed line). The various terms are defined in the text. Note that the most unstable mode which drives the system is located at $k_y = 0.6\ \mathrm{cm}^{-1}$ in both the insulating and conducting cases. The detailed balancing of terms and the behavior near $k_y = 0$ (inverse cascade) is different in the two cases.

Fig. 4 (Color online) Radial profiles of the azimuthal velocity, using Time Delay Estimation methods, obtained for B = 1000 G, P_{rf} = 1500 W, argon gas pressure of 3.2 mTorr. Red circles are for the IBC and the blue squares are for the CBC. The error bars show the standard deviation measured by three different pairs of probe tips.

Fig. 5 (Color online) Radial profiles of the Reynolds stress obtained for B = 1000 G, P_{rf} = 1500 W, argon gas pressure of 3.2 mTorr. Red circles are for the IBC and the blue squares are for CBC.

Fig. 6 Experimentally measured frequency spectrum of the floating potential, $\left|\Phi_{float}\right|^2$, at the radial location (r = 3.8 cm) corresponding to the maximum density gradient for (a) the IBC case and (b) the CBC case.

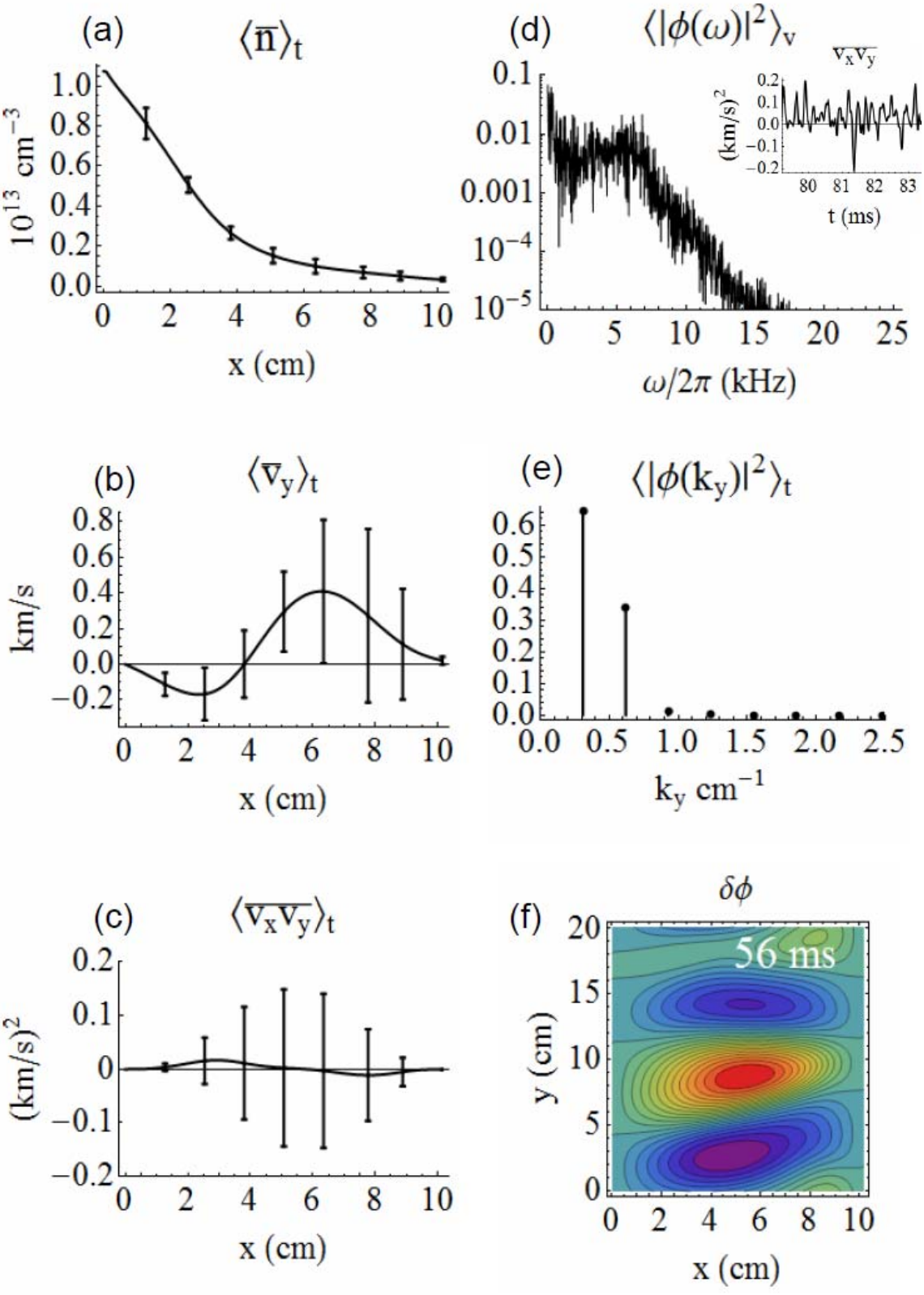
(a)
$\langle \overline{n} \rangle_t$
10^{13} cm^{-3}
x (cm)
(d)
$\langle |\phi(\omega)|^2 \rangle_v$
$\overline{v_x v_y}$
(km/s)^2
t (ms)
$\omega/2\pi$ (kHz)
(b)
$\langle \overline{v}_y \rangle_t$
km/s
x (cm)
(e)
$\langle |\phi(k_y)|^2 \rangle_t$
k_y cm^{-1}
(c)
$\langle \overline{v_x v_y} \rangle_t$
(km/s)^2
x (cm)
(f)
$\delta\phi$
56 ms
y (cm)
x (cm)

Fig. 1

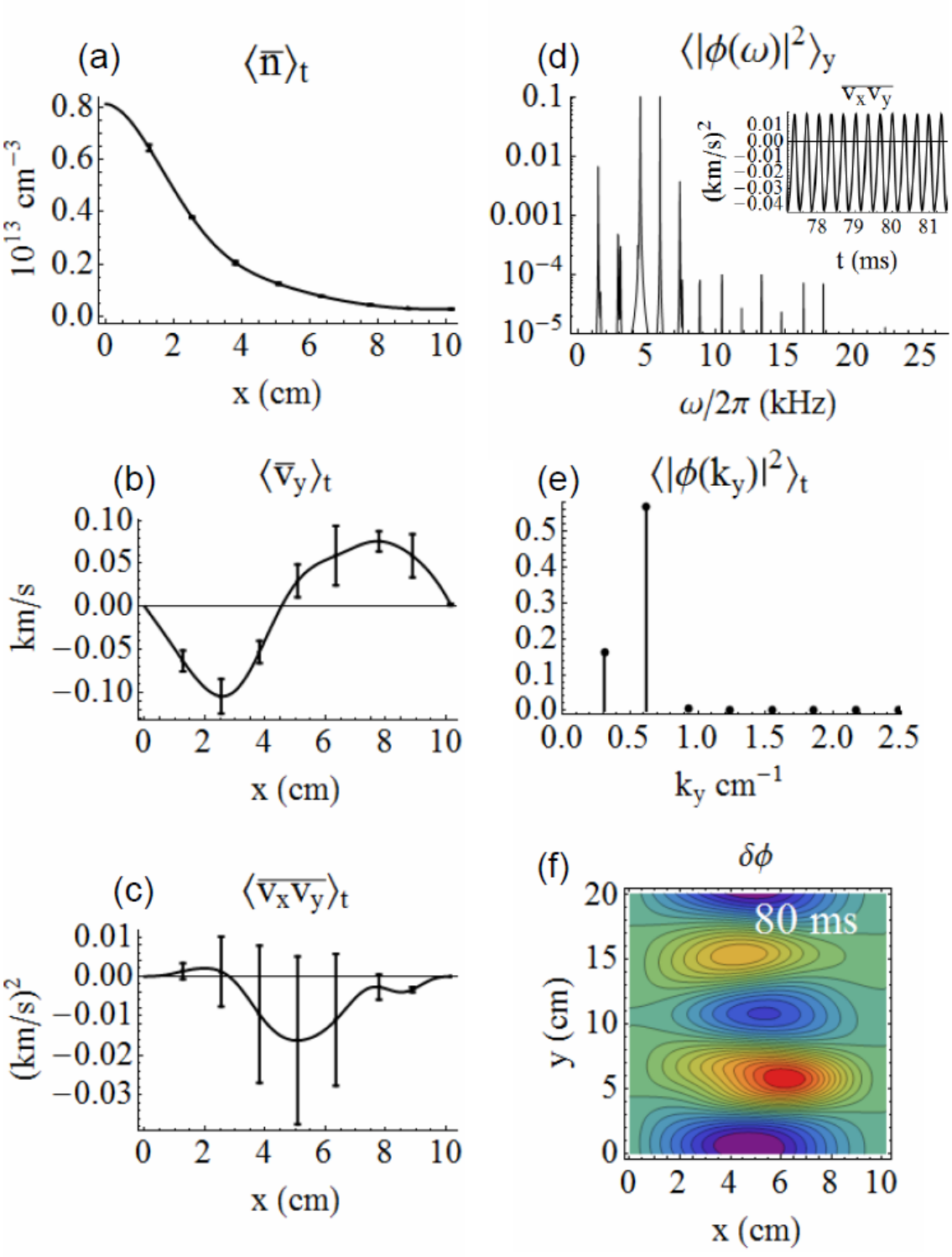
(a)
$\langle \overline{n} \rangle_t$
10^{13} cm^{-3}
x (cm)
(b)
$\langle \overline{v}_y \rangle_t$
km/s
x (cm)
(c)
$\langle \overline{v_x v_y} \rangle_t$
(km/s)^2
x (cm)
(d)
$\langle |\phi(\omega)|^2 \rangle_y$
$\overline{v_x v_y}$
(km/s)^2
t (ms)
$\omega/2\pi$ (kHz)
(e)
$\langle |\phi(k_y)|^2 \rangle_t$
k_y cm^{-1}
(f)
$\delta\phi$
80 ms
y (cm)
x (cm)

Fig. 2

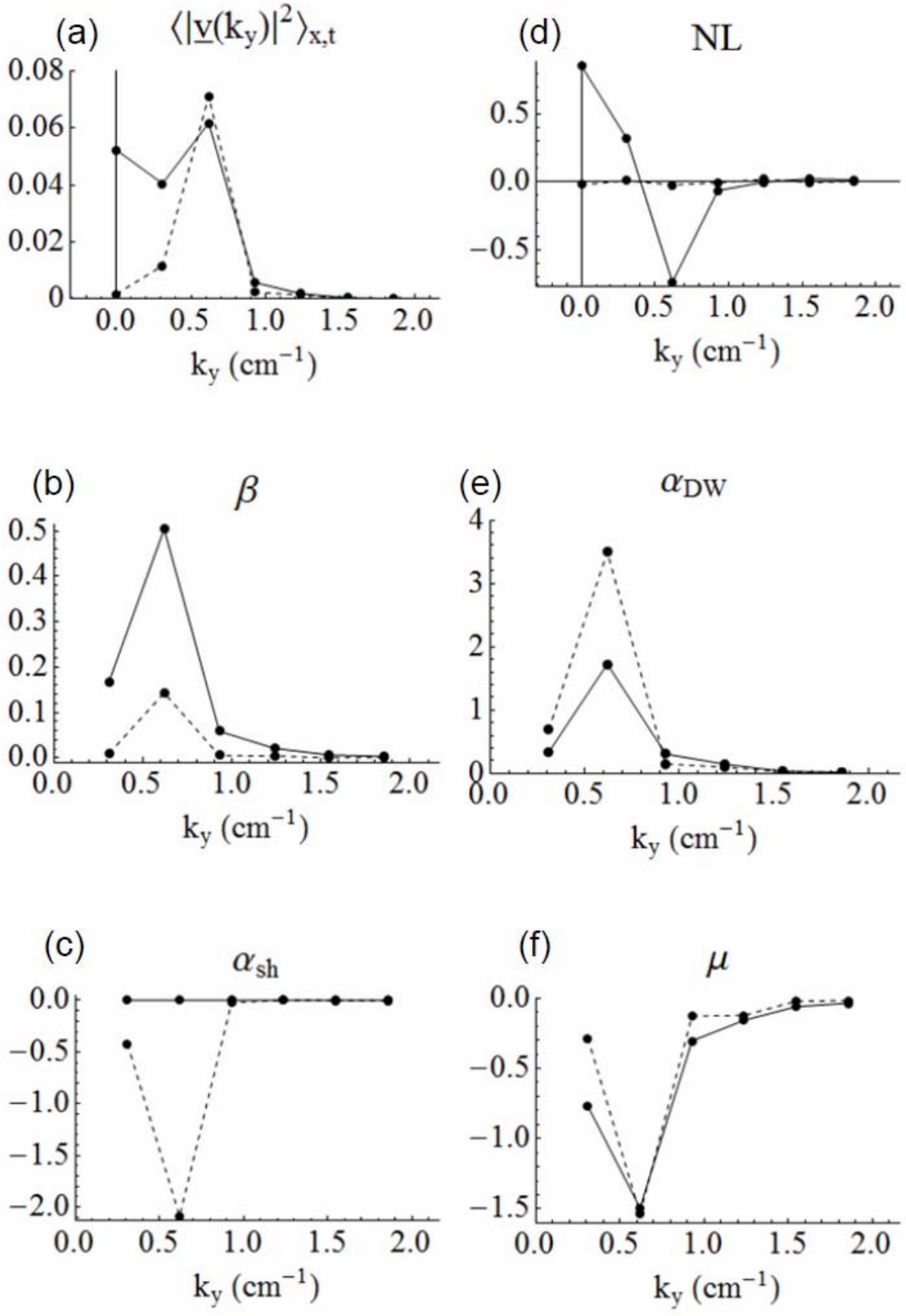
(a)
$\langle|\underline{v}(k_y)|^2\rangle_{x,t}$
0.08
0.06
0.04
0.02
0
0.0 0.5 1.0 1.5 2.0
k_y (cm^{-1})
(d)
NL
0.5
0.0
−0.5
0.0 0.5 1.0 1.5 2.0
k_y (cm^{-1})
(b)
β
0.5
0.4
0.3
0.2
0.1
0.0
0.0 0.5 1.0 1.5 2.0
k_y (cm^{-1})
(e)
α_{DW}
4
3
2
1
0
0.0 0.5 1.0 1.5 2.0
k_y (cm^{-1})
(c)
α_{sh}
0.0
−0.5
−1.0
−1.5
−2.0
0.0 0.5 1.0 1.5 2.0
k_y (cm^{-1})
(f)
μ
0.0
−0.5
−1.0
−1.5
0.0 0.5 1.0 1.5 2.0
k_y (cm^{-1})

Fig. 3

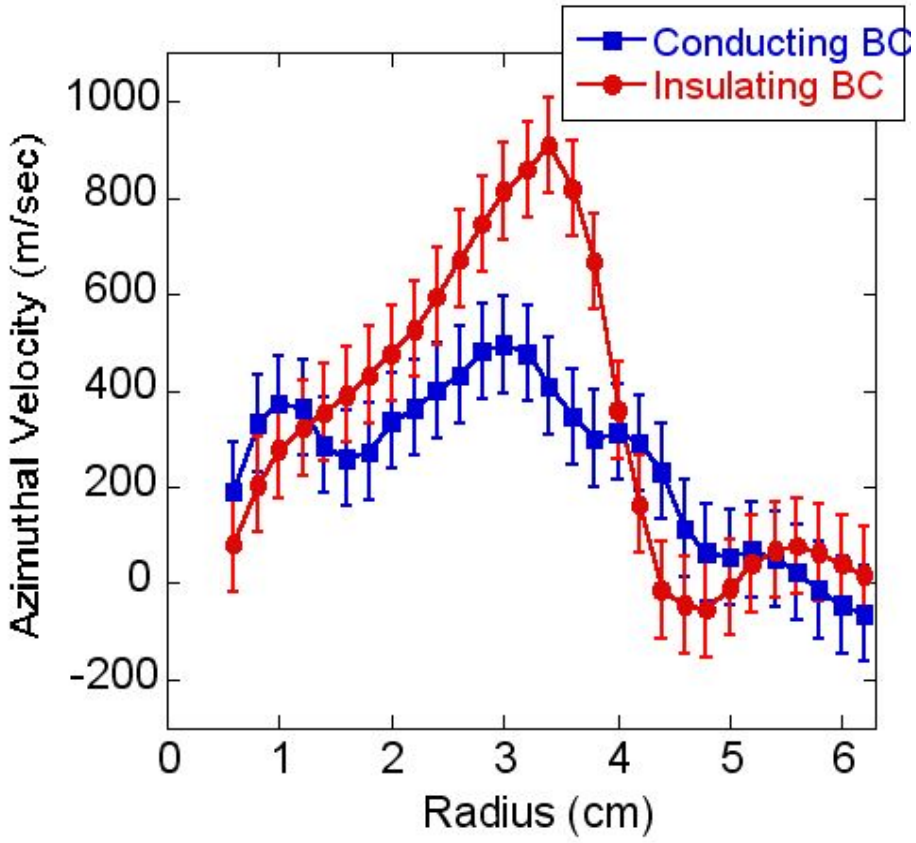
Conducting BC
Insulating BC
Azimuthal Velocity (m/sec)
1000
800
600
400
200
0
-200
0
1
2
3
4
5
6
Radius (cm)

Fig. 4

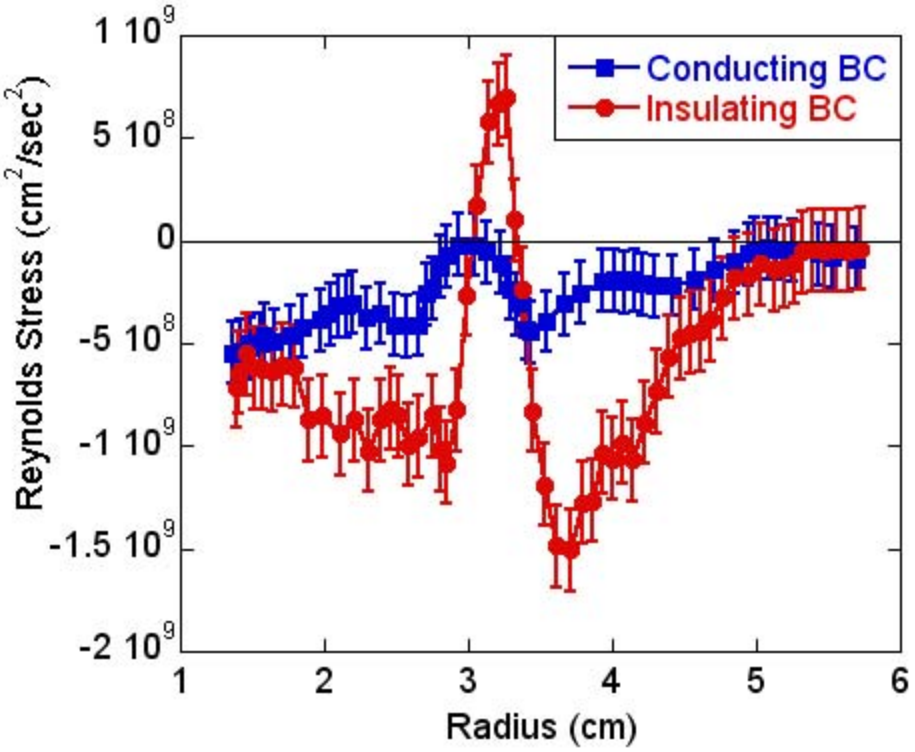
Conducting BC
Insulating BC
Reynolds Stress (cm^2/sec^2)
Radius (cm)
1 10^9
5 10^8
0
-5 10^8
-1 10^9
-1.5 10^9
-2 10^9
1
2
3
4
5
6

Fig. 5

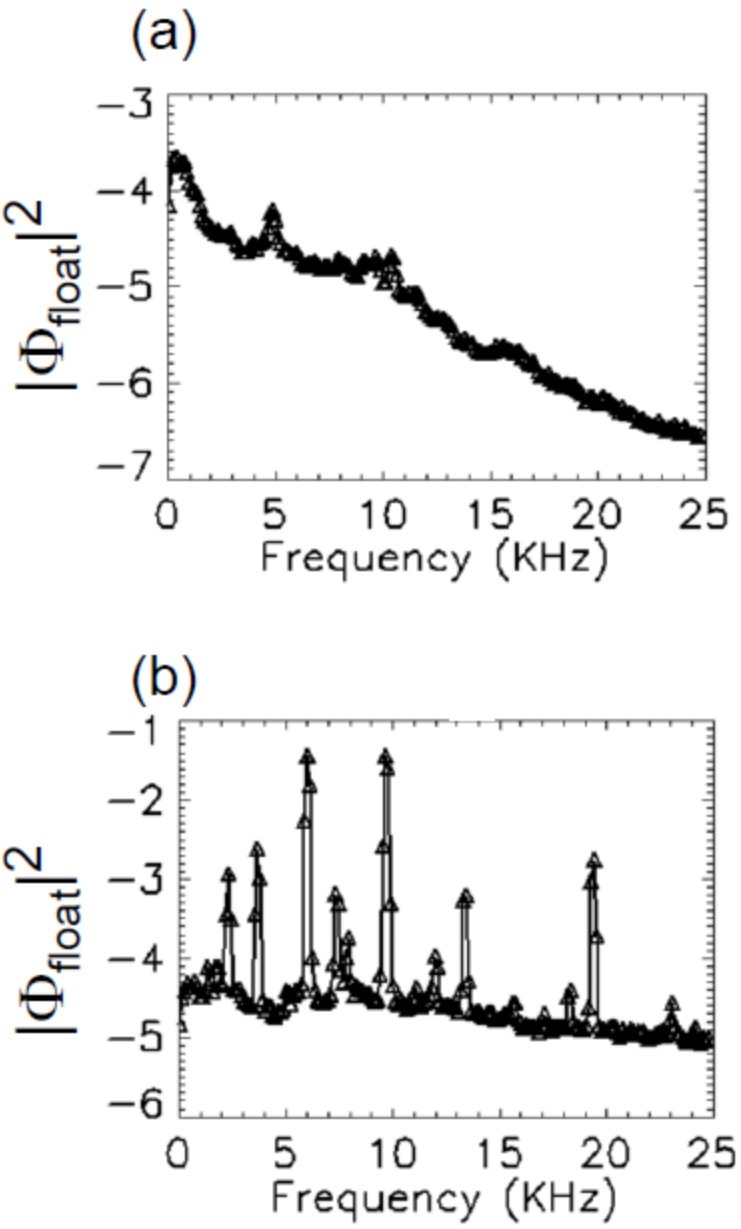
(a)
$|\Phi_{float}|^2$
−3
−4
−5
−6
−7
0
5
10
15
20
25
Frequency (KHz)
(b)
$|\Phi_{float}|^2$
−1
−2
−3
−4
−5
−6
0
5
10
15
20
25
Frequency (KHz)

Fig. 6

References

[1] S. J. Zweben, J. A. Boedo, O. Grulke, C. Hidalgo, B. LaBombard, R. J. Maqueda, P. Scarin, and J. L. Terry, Plasma Phys. Controlled Fusion **49**, S1 (2007).

[2] G. R. Tynan, A. Fujisawa and G. McKee, Plasma Phys. Control. Fusion **51**, 113001 (2009).

[3] P. W. Terry, Rev. Mod. Phys. **72**, 109 (2000).

[4] P. H. Diamond, A. Hasegawa and K. Mima, Plasma Phys.Control. Fusion **53**, 124001 (2011).

[5] M. J. Burin, G. R. Tynan, G. Y. Antar, N. A. Crocker, and C. Holland, Phys. Plasmas 12, 052320 (2005).

[6] T. A. Carter, Phys. Plasmas 13, 010701 (2006).

[7] O. Grulke, S. Ullrich, T. Windisch and T. Klinger, Plasma Phys. Control. Fusion 49 B247–B257 (2007).

[8] T. Windisch, O. Grulke, R. Schneider, and G. N. Kervalishvili, Contrib. Plasma Phys. **48**, 58 (2008).

[9] V. Naulin, T. Windisch and O. Grulke, Phys. Plasmas **15**, 012307 (2008).

[10] T. Windisch, O. Grulke, V. Naulin and T. Klinger, Plasma Phys. Control. Fusion **53**, 085001 (2011); T. Windisch, O. Grulke, V. Naulin and T. Klinger, Plasma Phys. Control. Fusion **53**, 124036 (2011).

[11] M. V. Umansky, P. Popovich, T. A. Carter, B. Friedman, and W. M. Nevins, Phys. Plasmas **18**, 055709 (2011).

[12] C. Holland, G. R. Tynan, J. H. Yu, A. James, D. Nishijima, M. Shimada and N. Taheri, Plasma Phys. Control. Fusion **49**, A109 (2007).

[13] N. Kasuya, M.Yagi, K. Itoh, and S-I Itoh, Phys. Plasmas **15**, 052302 (2008).

[14] W. B. Kunkel and J. U. Guillory, in *Proceedings of the Seventh International Conference on Phenomena in Ionized Gases*, Belgrade, 1965, edited by B. Perovic and D. Tosić (Gradjevinska Knjiga Publishing House, Belgrade, Yugoslavia, 1966), Vol. **II**, p. 702.

[15] A. V. Nedospasov, V. G. Petrov, and G. N. Fidel'man, Nucl. Fusion **25**, 21 (1985).

[16] H.L. Berk, R.H. Cohen, D.D. Ryutov, Yu.A. Tsidulko and X.Q. Xu, Nucl. Fusion **33**, 263 (1993).

[17] O. E. Garcia, N. H. Bian and W. Fundamenski, Phys. Plasmas 13, 082309 (2006).

[18] I. Furno, C. Theiler, D. Lançon, A. Fasoli, D. Iraji, P. Ricci, M. Spolaore and N. Vianello, Plasma Phys. Control. Fusion **53**, 124016 (2011).

[19] S. Chakraborty Thakur, M. Xu, P. Manz, N. Fedorczak, C. Holland and G. R. Tynan, submitted for publication in Phys. Plasmas (2012) .

[20] J. R. Myra, D. A. Russell, and D. A. D'Ippolito, Phys. Plasmas **15**, 032304 (2008).

[21] D. A. Russell, J.R. Myra and D.A. D'Ippolito, Phys. Plasmas **16**, 122304 (2009).

[22] J.R. Myra, D.A. Russell, D.A. D'Ippolito, J-W. Ahn, R. Maingi, R.J. Maqueda, and J. Boedo, Phys. Plasmas **18**, 012305 (2011).

[23] D. A. Russell, J. R. Myra and D. A. D'Ippolito, T. L. Munsat and Y. Sechrest, R. J. Maqueda, D. P. Stotler, S. J. Zweben and the NSTX Team, Phys. Plasmas **18**, 022306 (2011).

[24] S. I. Krasheninnikov, D. A. D'Ippolito and J. R. Myra, J. Plasma Phys. **74**, 679 (2008).

[25] D. A. D'Ippolito, J. R. Myra and S. J. Zweben, Phys. Plasmas **18**, 060501 (2011).

[26] J.R. Myra, D.A. Russell, D.A. D'Ippolito, J-W. Ahn, R. Maingi, R.J. Maqueda, D.P. Lundberg, D.P. Stotler, S.J. Zweben, and M. Umansky, J. Nucl. Mater. **415**, S605 (2011).

[27] M. Wakatani and A. Hasegawa, Phys. Fluids **27**, 611 (1984); A. Hasegawa and M. Wakatani Phys. Rev. Lett. **59**, 1581 (1987).

[28] Z. Yan, M. Xu, P. H. Diamond, C. Holland, S. H. Müller, G. R. Tynan, and J. H. Yu, Phys. Rev. Lett. **104**, 065002 (2010).

[29] M. Xu, G. R. Tynan, C. Holland, Z. Yan, S. H. Müller, and J. H. Yu, Phys. Plasmas **17**, 032311 (2010).

[30] Z. Yan, G. R. Tynan, C. Holland, M. Xu, S. H. Muller and J. H. Yu, Phys. Plasmas **17**, 012302 (2010).

[31] Z. Yan, G. R. Tynan, C. Holland, M. Xu, S. H. Muller and J. H. Yu, Phys. Plasmas **17**, 032302 (2010).